LETTER

doi:10.1038/nature14262

Ongoing hydrothermal activities within Enceladus

Hsiang-Wen Hsu[1]*, Frank Postberg[2,3]*, Yasuhito Sekine[4]*, Takazo Shibuya[5], Sascha Kempf[1], Mihály Horányi[1], Antal Juhász[1,6], Nicolas Altobelli[7], Katsuhiko Suzuki[8], Yuka Masaki[8], Tatsu Kuwatani[9], Shogo Tachibana[10], Sin-iti Sirono[11], Georg Moragas-Klostermeyer[3] & Ralf Srama[3]

Detection of sodium-salt-rich ice grains emitted from the plume of the Saturnian moon Enceladus suggests that the grains formed as frozen droplets from a liquid water reservoir that is, or has been, in contact with rock[1,2]. Gravitational field measurements suggest a regional south polar subsurface ocean of about 10 kilometres thickness located beneath an ice crust 30 to 40 kilometres thick[3]. These findings imply rock–water interactions in regions surrounding the core of Enceladus. The resulting chemical 'footprints' are expected to be preserved in the liquid and subsequently transported upwards to the near-surface plume sources, where they eventually would be ejected and could be measured by a spacecraft[4]. Here we report an analysis of silicon-rich, nanometre-sized dust particles[5–8] (so-called stream particles) that stand out from the water-ice-dominated objects characteristic of Saturn. We interpret these grains as nanometre-sized SiO_2 (silica) particles, initially embedded in icy grains emitted from Enceladus' subsurface waters and released by sputter erosion in Saturn's E ring. The composition and the limited size range (2 to 8 nanometres in radius) of stream particles indicate ongoing high-temperature (>90 °C) hydrothermal reactions associated with global-scale geothermal activity that quickly transports hydrothermal products from the ocean floor at a depth of at least 40 kilometres up to the plume of Enceladus.

Dust dynamics provide diagnostic information about the origin of the observed dust populations. The dynamical properties of Saturnian stream particles show characteristics inherited from Saturn's diffuse E ring[7]. Considering the long-term evolution of the E ring and dust–plasma interactions, our dynamical analysis reproduces the observed characteristics, confirming their E-ring origin (Methods). Enceladus is the source of the E ring and hence the ultimate source of stream particles, allowing Enceladus to be probed using stream particle measurements.

Co-added mass spectra of selected Saturnian stream particles detected by Cassini's Cosmic Dust Analyser (CDA)[9] (Fig. 1) show silicon as the only highly significant particle constituent. Oxygen is the other abundant possible particle mass line but is also a minor but frequent target contaminant[10]. The contribution of particle material to the oxygen signal is difficult to assess, but its intensity is in agreement with at least a fractional contribution from silicates (Methods). Remarkably, only traces (at most) of metals are found to contribute to the particle composition, indicating that the stream particle spectra are not in agreement with those of typical rock-forming silicate minerals (that is, olivine or pyroxene). The data are in agreement solely with extremely metal-poor (or metal-free) silicon-bearing compounds, of which, besides elemental Si, only SiO_2 and SiC are of cosmochemical relevance[11]. Considering that Si and SiC are highly unlikely to be emitted in significant quantities from a planetary body, we conclude that the dominant, if not sole, constituent of most stream particles must therefore be SiO_2. Quantitative mass spectra analysis indicates a radius of $r_{max} = 6–9$ nm for the largest stream particles (Methods). This is in excellent agreement with the upper particle size limit independently inferred from dynamical simulations ($r_{max} \approx 8$ nm)[7].

The spontaneous, homogeneous nucleation of nanometre-sized colloidal silica is a unique property of the silica–water system. We consider this as the production mechanism of the observed silica nanoparticles because of (1) the existence of a subsurface ocean in contact with rock and (2) the improbability of homogeneous fragmentation of pure bulk silica into particles with radii exclusively below 10 nm within Enceladus. Only a rock-related, bottom-up formation process is plausible. Colloidal silica nanoparticles form with initial radii of 1–1.5 nm when the solution becomes supersaturated[12]. In moderately alkaline solutions (pH 7.5–10.5) with low electrolyte concentration, the charge state of silica nuclei allows colloidal silica nanoparticles to nucleate and grow by addition of dissolved silica as well as by Ostwald ripening[12,13]. Above about pH 10.5, silica solubility becomes too high to maintain a stable colloidal phase[12]. Laboratory experiments show that after hours to days in a supersaturated solution with a slightly alkaline pH and at various ionic strengths, colloidal silica grows to radii of 2–6 nm (refs 14–17), which is in good agreement with CDA measurements.

Both measurements—mass spectra and the narrow size distribution—indicate silica nanoparticles but may not provide unequivocal proof

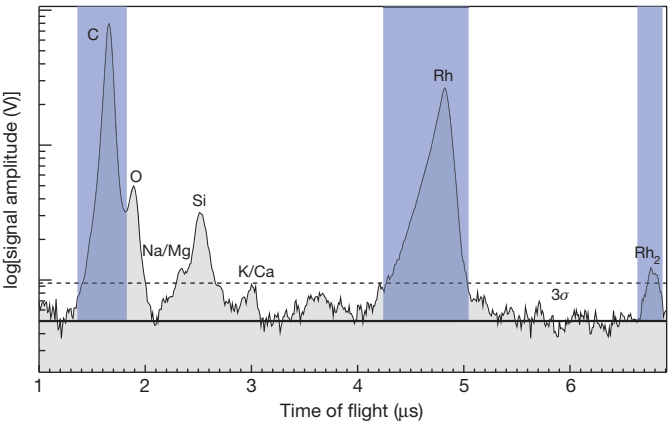

Figure 1 | Identifying particle constituents. Shown is a co-added impact ionization mass spectrum from 32 selected Saturnian stream particle spectra with the strongest Si^+ signals. As expected, the impacts produce more ions from the CDA's target material (Rh^+ and Rh_2^+; blue areas) and the target contaminants[6,10] (C^+, H^+; blue areas, H^+ not shown) than from the nanoparticle itself. Ions O^+ and Si^+ are the most abundant potential particle mass lines. Na^+/Mg^+ (solidus indicates the two species can not be distinguished) form the only other potential particle mass line with a signal-to-noise ratio above 3σ (dashed line; σ, standard deviation). The particle composition agrees best with pure silica when the target impurities and the impact ionization process are taken into account (Methods).

[1]Laboratory for Atmospheric and Space Physics, University of Colorado, Boulder, Colorado 80303, USA. [2]Institut für Geowissenschaften, Universität Heidelberg, 69120 Heidelberg, Germany. [3]Institut für Raumfahrtsysteme, Universität Stuttgart, 70569 Stuttgart, Germany. [4]Department of Complexity Science and Engineering, University of Tokyo, Kashiwa 277-8561, Japan. [5]Laboratory of Ocean–Earth Life Evolution Research, JAMSTEC, Yokosuka 237-0061, Japan. [6]Institute for Particle and Nuclear Physics, Wigner RCP, 1121 Budapest, Hungary. [7]European Space Agency, ESAC, E-28691 Madrid, Spain. [8]Research and Development Center for Submarine Resources, JAMSTEC, Yokosuka 237-0061, Japan. [9]Graduate School of Environmental Studies, Tohoku University, Sendai 980-8579, Japan. [10]Department of Natural History Sciences, Hokkaido University, Sapporo 060-0810, Japan. [11]Graduate School of Environmental Sciences, Nagoya University, Nagoya 464-8601, Japan.
*These authors contributed equally to this work.

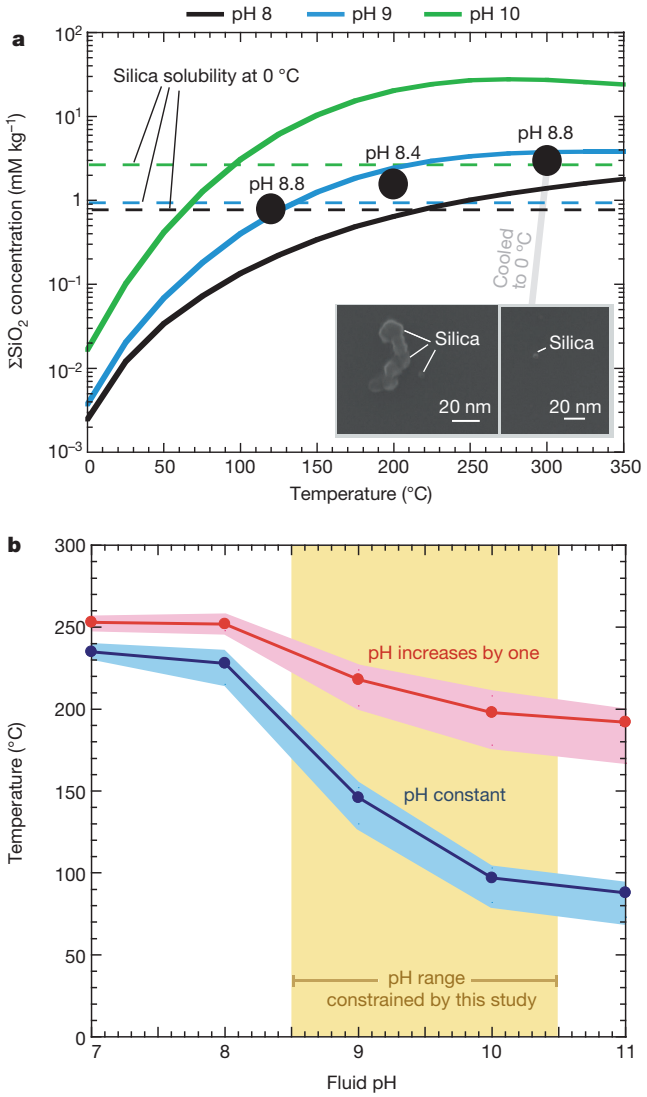

Figure 2 | Minimum temperatures for formation of silica nanoparticles. **a**, Solid lines show ΣSiO_2 of a serpentine–talc/saponite buffer equilibrium as a function of temperature (*x* axis) and pH (line colour: see key above). This buffer system is consistent with the measured ΣSiO_2 in fluid samples of the hydrothermal experiments using an orthopyroxene and olivine powder mixture at 400-bar pressure (filled black circles annotated with *in situ* pH values; Methods). Dashed lines show the 0 °C silica solubility at the respective pH. The difference between the solid and dashed lines determines the amount of ΣSiO_2 available for silica nanoparticle formation at the respective pH. Insets, images of silica nanoparticles formed in cooled solutions. **b**, Relationships between minimum hydrothermal fluid temperatures and fluid pH for silica nanoparticle formation. Red and blue colours represent results with increasing and fixed pH, respectively, upon cooling and mixing with seawater. Data points show results for Na^+ concentration 0.1 mol kg^{-1} and pressure 30 bar; shaded areas represent the uncertainties in Na^+ concentrations (0.05–0.3 mol kg^{-1}) and pressure (10–80 bar; ref. 3).

individually. However, nanosized silica remains as the only plausible interpretation of the stream particle measurements when results from these two independent analysis methods are incorporated. Moreover, the relation between the stability of silica nanoparticles and solvent alkalinity matches the pH range of the liquid plume source(s) (about 8.5–9), as independently inferred from the composition of emitted salt-rich ice grains[1,2].

We can now use silica nanoparticles as a thermometer for the subsurface ocean floor of Enceladus, assuming that such particles form owing to SiO_2 solubility reduction during a temperature reduction in cooling water[17,18]. This is the most common way for silica nanoparticles to form on Earth, and is frequently observed in alkaline hydrothermal fluids[12,17–19]. To determine the relation of silica concentration versus solution temperature applicable to Enceladus, long-term rock–water interaction experiments were conducted. A pressurized solution of $NaHCO_3$ and NH_3 in water was brought into contact with powdered primordial minerals (70% olivine and 30% pyroxene) at various temperatures and for several months (Methods). Hydrothermal alterations produced secondary minerals typically found in carbonaceous chondrites, including serpentine, talc/saponite and magnetite. Our experimental results (Fig. 2a) show that the total SiO_2 concentration in fluids ($\Sigma SiO_2 = SiO_2(aq.) + HSiO_3^- + NaSiO_3(aq.)$) in contact with these secondary minerals is controlled by a serpentine–talc/saponite buffer system: that is, serpentine + $2SiO_2(aq.) \leftrightarrow$ talc/saponite + H_2O. This allows us to calculate the minimum temperature required for silica nanoparticle formation on cooling of the hydrothermal fluids—that is, the reaction temperature at which ΣSiO_2 exceeds the solubility of amorphous silica at 0 °C for a given pH. Assuming the fluid pH remains constant on cooling, the reaction temperature must reach ~90 °C at pH 10.5, or a higher temperature if the fluid pH is below 10.5 (Fig. 2b). Because silica solubility increases with fluid alkalinity, the minimum temperature allowing silica nanoparticle formation on subsequent cooling rises to ~190 °C at pH 10.5 if the hydrothermal fluid pH were to increase by one when mixing with the subsurface ocean water (Methods and ref. 20).

It is not clear how steep the temperature gradient across the subsurface ocean is. However, the ocean is most likely to be convective if the minimum temperature allowing silica nanoparticle formation on subsequent cooling (that is, > 90 °C) at the rock–water interface is achieved. We believe that most silica nucleation and initial growth would occur when the hydrothermal fluids reach the relatively cold ocean water at the ocean floor. The growth of silica nanoparticles may continue as the hydrothermal fluids ascend (Fig. 3).

For comparison, the average concentration of silica nanoparticles in their icy E-ring 'carrier grains' can be estimated using the measured and modelled stream particle production rate (Fig. 4 and Methods). Albeit with large uncertainties, a conservative lower limit still requires the formation of 150 p.p.m. of silica nanoparticles, equivalent to a solution supersaturated by about 2.5 mM SiO_2, which was available to form the observed nanoparticles. Such a high nanosilica abundance requires a high temperature gradient at a pH of at least 8.5, and cannot be explained solely by incorporation of dissolved silica on freezing of water droplets in the vents[2]. The high abundance and specific sizes of stream particles both indicate that they existed in colloidal form before their integration into ice grains.

The existence of silica nanoparticles also provides strict constraints on the salinity of Enceladus' subsurface waters because silica colloids aggregate and precipitate quickly at high ionic strength[12,13]. The critical coagulation concentration of NaCl at pH 9 is 2% or ~0.3 M (1.5% or ~0.2 M at pH 10, 4% or ~0.6 M at pH 8)[13]. This sets an upper salinity limit of about 4% for the location where silica nanoparticles form at depth, as well as for the near-surface plume sources, and corresponds to the lower salinity limit of 0.5% derived earlier[1]. Partial freezing of the water would increase the salinity and would result in immediate silica precipitation[19], suggesting that the observed silica nanoparticles have never 'seen' a brine. This also implies that the observed silica nanoparticles were produced during the present active phase of Enceladus.

The growth of colloidal particles sets another constraint on the lifetime of the silica nanoparticles. For example, through Ostwald ripening[21], nanosilica would grow to micrometre-sized grains within a few thousand years or less (Methods). The observed radii, below 10 nm, imply the continuous and relatively fast upward transportation of hydrothermal products (see, for example, ref. 22), from ongoing hydrothermal activities in the subsurface ocean to the plume sources close to the surface, over months to several years at most (Methods).

Our results show that two very different dust populations detected by Cassini—that is, micrometre-sized ice grains[1,2,4,23,24] and nanometre-sized

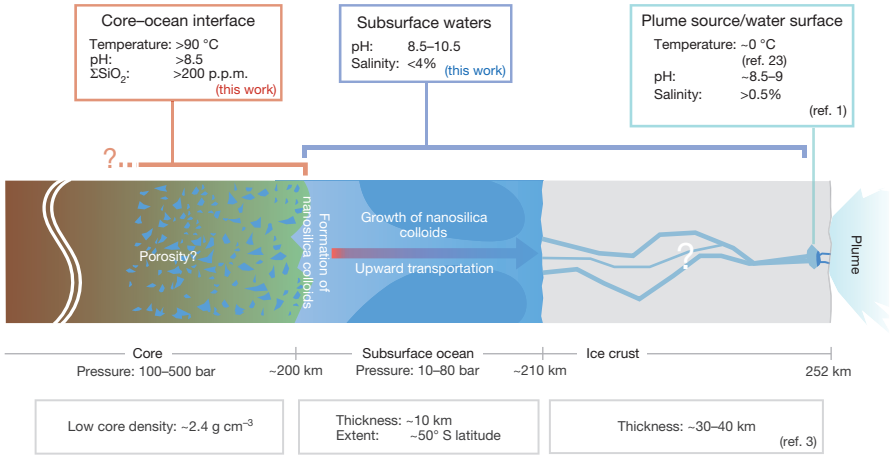

Figure 3 | A schematic of Enceladus' interior. The internal structure and conditions of Enceladus beneath its south polar region derived from this and previous work. The main components (core, subsurface ocean, ice crust and plume) are shown left to right; top row gives temperature and chemical properties of each component, middle row shows schematic structure, and bottom row gives physical properties. Distances labelling the grey line below the middle row are distances from the centre of Enceladus towards its south pole (not to scale).

silica stream particles—in fact have the same origin but probe the conditions of the subsurface water of Enceladus at different depths: the silica nanoparticles probe the pH, salinity and water temperature at the bottom of Enceladus' ocean, while the micrometre-sized ice dust grains reveal composition and thermal dynamical processes at near-surface liquid plume sources and in the vents[1,2,23] (Fig. 3). The current plume activity is probably not superficial but a large, core-to-surface-scale process. The low core densities implied by Cassini's gravitational field measurements[3] as well as the low pressure of the mantle resting on the core[25] are in good agreement with a porous core. This would allow water to percolate through it, providing a huge surface area for rock–water interactions, and the high temperatures (>90 °C) implied by our observations might occur deep inside Enceladus' core.

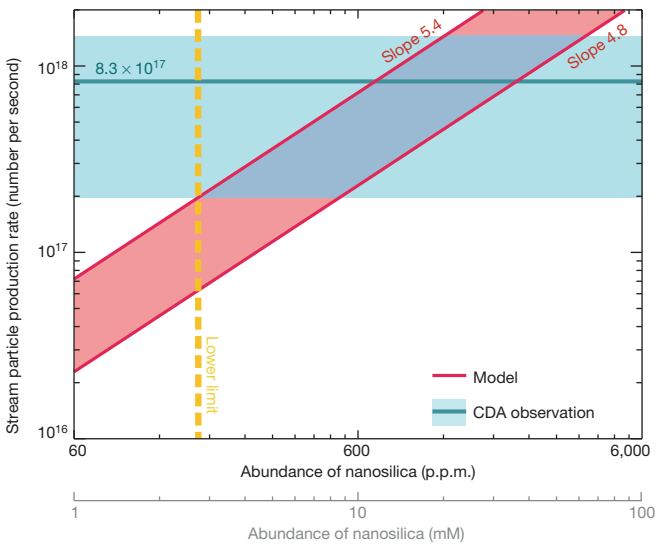

Figure 4 | Concentration of silica nanoparticles in E-ring grains. The mass fraction of silica nanoparticles in E-ring ice grains is estimated by comparing the production rates derived from the dynamical model (sloping red lines) and CDA measurements (blue horizontal line and shaded region). We assume that the stream particle release rate is directly proportional to the E-ring sputtering erosion rate. The steeper the power-law size distribution slope (μ), the larger the total surface area of E-ring grains and thus the higher the production rate of silica nanoparticles. The lower limit for the nanosilica mass fraction is ~150 p.p.m. (equivalent to 2.5 mM shown in the lower x axis) with $\mu = 5.4$ (yellow dashed line)[24].

Online Content Methods, along with any additional Extended Data display items and Source Data, are available in the online version of the paper; references unique to these sections appear only in the online paper.

Received 29 November 2013; accepted 26 January 2015.

1. Postberg, F. *et al.* Sodium salts in E-ring ice grains from an ocean below the surface of Enceladus. *Nature* **459,** 1098–1101 (2009).
2. Postberg, F., Schmidt, J., Hillier, J., Kempf, S. & Srama, R. A salt-water reservoir as the source of a compositionally stratified plume on Enceladus. *Nature* **474,** 620–622 (2011).
3. Iess, L. *et al.* The gravity field and interior structure of Enceladus. *Science* **344,** 78–80 (2014).
4. Hillier, J. K. *et al.* The composition of Saturn's E ring. *Mon. Not. R. Astron. Soc.* **377,** 1588–1596 (2007).
5. Kempf, S. *et al.* High-velocity streams of dust originating from Saturn. *Nature* **433,** 289–291 (2005).
6. Kempf, S. *et al.* Composition of Saturnian stream particles. *Science* **307,** 1274–1276 (2005).
7. Hsu, H.-W. *et al.* Stream particles as the probe of the dust-plasma-magnetosphere interaction at Saturn. *J. Geophys. Res.* **116,** A09215 (2011).
8. Hsu, H.-W., Krüger, H. & Postberg, F. in *Nanodust in the Solar System: Discoveries and Interpretations* (eds Mann, I., Meyer-Vernet, N. & Czechowski, A.) 77–117 (Springer Astrophysics and Space Science Library, Vol. 385, 2012).
9. Srama, R. *et al.* The Cassini cosmic dust analyzer. *Space Sci. Rev.* **114,** 465–518 (2004).
10. Postberg, F. *et al.* Discriminating contamination from particle components in spectra of Cassini's dust detector CDA. *Planet. Space Sci.* **57,** 1359–1374 (2009).
11. Ming, T. *et al.* Meteoritic silicon carbide and its stellar sources — implications for galactic chemical evolution. *Nature* **339,** 351–354 (1989).
12. Iler, R. K. *The Chemistry of Silica* (Wiley & Sons, 1979).
13. Allen, L. H. & Matijević, E. Stability of colloidal silica, I. Effect of simple electrolytes. *J. Colloid Interface Sci.* **31,** 287–296 (1969).
14. Icopini, G. A., Brantley, S. L. & Heaney, P. J. Kinetics of silica oligomerization and nanocolloid formation as a function of pH and ionic strength at 25°C. *Geochim. Cosmochim. Acta* **69,** 293–303 (2005).
15. Conrad, C. F. *et al.* Modeling the kinetics of silica nanocolloid formation and precipitation in geologically relevant aqueous solutions. *Geochim. Cosmochim. Acta* **71,** 531–542 (2007).
16. Tobler, D. J., Shaw, S. & Benning, L. G. Quantification of initial steps of nucleation and growth of silica nanoparticles: an *in-situ* SAXS and DLS study. *Geochim. Cosmochim. Acta* **73,** 5377–5393 (2009).
17. Tobler, D. J. & Benning, L. G. *In situ* and time resolved nucleation and growth of silica nanoparticles forming under simulated geothermal conditions. *Geochim. Cosmochim. Acta* **114,** 156–168 (2013).
18. Herzig, P. M. *et al.* Hydrothermal silica chimney fields in the Galapagos Spreading Center at 86° W. *Earth Planet. Sci. Lett.* **89,** 261–272 (1988).
19. Channing, A. & Butler, I. B. Cryogenic opal-A deposition from Yellowstone hot springs. *Earth Planet. Sci. Lett.* **257,** 121–131 (2007).
20. Zolotov, M. Y. Aqueous fluid composition in CI chondritic materials: chemical equilibrium assessments in closed systems. *Icarus* **220,** 713–729 (2012).
21. Sirono, S. Differentiation of silicates from H_2O ice in an icy body induced by ripening. *Earth Planets Space* **65,** 1563–1568 (2013).
22. Matson, D. L., Castillo-Rogez, J. C., Davies, A. G. & Johnson, T. V. Enceladus: a hypothesis for bringing both heat and chemicals to the surface. *Icarus* **221,** 53–62 (2012).
23. Schmidt, J., Brilliantov, N., Spahn, F. & Kempf, S. Slow dust in Enceladus' plume from condensation and wall collisions in tiger stripe fractures. *Nature* **451,** 685–688 (2008).

24. Kempf, S. *et al.* The E ring in the vicinity of Enceladus. I. Spatial distribution and properties of the ring particles. *Icarus* **193,** 420–437 (2008).
25. Malamud, U. & Prialnik, D. Modeling serpentinization: applied to the early evolution of Enceladus and Mimas. *Icarus* **225,** 763–774 (2013).

Acknowledgements We acknowledge support from the CDA team, the Cassini project, and NASA. This research was partly supported by Grants-in-Aid for Scientific Research from the Ministry of Education, Culture, Sports, Science and Technology, Japan, by the Japan Society for the Promotion of Science, and by the Astrobiology Program of the National Institutes of Natural Sciences, Japan. This work was partly supported by the DLR grant 50 OH1103. We thank J. Schmidt, M. Y. Zolotov and D. J. Tobler for discussions, and E. S. Guralnick, J. K. Hillier, A. Rasca and T. Munsat for advice on writing this Letter. Y.S. thanks A. Okubo for her technical help in taking FE-SEM images.

Author Contributions H.-W.H., F.P. and Y.S. outlined the study and wrote the Letter. H.-W.H. performed the CDA dynamic analyses with assistance from A.J., M.H. and S.K.; F.P. and S.K. performed the CDA composition analyses; S.K., G.M.-K. and R.S. performed the CDA measurements and initial data processing; F.P. and N.A. performed the CDA mass spectra data acquisition and data reduction; Y.S. performed the experiments and calculations simulating Enceladus' ocean conditions; T.S. designed the hydrothermal experiments and the analysis system; S.T. synthesized starting minerals for the experiments; K.S., Y.M. and T.K. contributed to performing fluid and solid analyses in the experiments; and S.-i.S. estimated the lifetime of silica nanoparticles in Enceladus' ocean. All authors discussed the results and commented on the manuscript.

Author Information Reprints and permissions information is available at www.nature.com/reprints. The authors declare no competing financial interests. Readers are welcome to comment on the online version of the paper. Correspondence and requests for materials should be addressed to H.-W.H. (sean.hsu@lasp.colorado.edu).

METHODS

Dynamics analysis. The dynamical properties derived from nanodust–solar wind interactions (ejection speed: 50–200 km s^{-1}, charge-to-mass ratio: 1,000–20,000 C kg^{-1}, or 2–8 nm in radius assuming +5 V surface potential) links stream particles to an ejection region (ER) at ~8 R_S (R_S is the Saturn radius, 60,268 km) from Saturn[7]. The ER is defined as the region where charged nanoparticles start to gain energy from the co-rotation electric field to escape from the gravity of Saturn. Considering the energy conservation, the ER distribution thus represents the distribution of stream particles' dynamical properties as they are ejected from the system (equation (5) in ref. 7) and reflects the effects of the dust charging process as well as the source location[7]. The ER peak location indicates that their source extends from the inner system to over 8 R_S with strength decreasing outward[7]. It was therefore proposed that stream particles are nanometre-sized Si-rich inclusions in E-ring ice grains released through plasma sputtering erosion[7], as such sputtering is more corrosive on water ice than on Si-bearing minerals[26]. Enceladus is the dominant source of E-ring ice grains[27], suggesting that stream particles also originated from Enceladus.

One major difference between the E ring and other tentative sources (for example, Saturn's main rings and moons) is the vertical extension. E-ring grains can obtain significant inclination because of solar radiation pressure as well as gravitational perturbations from embedded moons[24,28,29]. Nanoparticles released from the E ring would inherit the inclination, as the magnetic field of Saturn aligns well with its rotation axis[30,31]. To examine the proposed hypothesis, we adopt numerical simulations to reconstruct the emission patterns of the Saturnian stream particles, as described below:

The sputtering mass loss rate of E-ring grains. Trajectories of ice grains with initial radius, r, between 0.1 and 5 μm from the dynamics model[29] are used to reconstruct the E-ring profile. E-ring grains follow a power-law size distribution, $n(r) \propto (r/r_0)^{-\mu}$, where r is the grain radius and μ ranges from 4.8 to 5.4 (ref. 24). Weighted with the initial size distribution and normalized to the dust density recorded at the orbit of Enceladus[24], the simulated trajectories are binned to a two-dimensional, axially symmetric dust density map (Extended Data Fig. 1a).

The dust size distribution and the mean dust–plasma relative speed are used to calculate the sputtering mass loss rate of E-ring grains at a given torus segment (ρ, z), expressed by

$$\dot{m}(\rho,z) = \int \Phi_{\mathrm{sput}}(\rho,z) \times A(r,\rho,z) \times m_{H_2O}\,\mathrm{d}r$$

where $A(r,\rho,z)$ is the surface area of E-ring grains with radius r in a given torus segment, ρ and z are the distance to the rotation axis of Saturn and to the ring plane, respectively, and m_{H_2O} is the mass of a water molecule. The sputtering yield (Φ_{sput}) of icy surface in Saturn's magnetosphere is governed by the elastic nuclear collisions from the thermal magnetospheric plasma ions[32–34] and can be written (equation (4) in ref. 33) as:

$$\Phi_{\mathrm{sput}}(\rho,z) = \bar{g}\frac{u(\rho,z) \times n_i(\rho,z)}{4} \times Y(E_i,0),$$

$$\bar{g} = \frac{2}{1-x}\left[1-(\cos\theta_m)^{1-x}\right],$$

$$x \approx 0.3 + 0.13\ln(m_i)$$

where $u(\rho, z)$ is the relative speed between E-ring grains and the magnetospheric plasma ions, $n_i(\rho, z)$ is the plasma ion density, and $m_i = m_{H_2O}$ We use an *ad hoc* plasma model built based on the Cassini measurements[7]. $\theta_m = 80^\circ$ is the ion incident angle beyond which the sputtering yield rapidly decreases[33]. $Y(E_i, 0)$ is the plasma ion sputtering yield of water ice[33,34]. The resulting E-ring mass loss rate is shown in Extended Data Fig. 1b.

Stream particle production rate. This is defined as the amount of escaping nanosilica particles per unit time. Under the assumption that the stream particle production is proportional to the E-ring ice mass loss rate ($\dot{m}$), the production rate (w) is written as:

$$w(r_{sp},\rho,z) = w'(r_{sp},\rho,z) f_{sp} f_{eff}, \quad (1)$$

$$w'(r_{sp},\rho,z) = \frac{\dot{m}(\rho,z)}{m_{sp}(r_{sp})} P_{mass}(r_{sp}) P_{eject}(r_{sp},\rho,z) \quad (2)$$

where f_{sp} is the mass ratio of silica nanoparticle with respect to the water ice in E-ring grains. f_{eff} is the efficiency of nanosilica release via the plasma sputtering process, which depends on the location distribution of nanosilica particles within the ice grain as well as the efficiency of plasma sputtering erosion processes. w', r_{sp}, m_{sp}, P_{mass}, P_{eject} are the normalized production rate, the radius, the mass, the mass distribution function, and the ejection probability of nanosilica stream particles, respectively. Based on the derived size range[7], we assume that stream particles follow a Gaussian distribution with a mean at 4 nm and variance of 2 nm. P_{eject} is calculated from the nanodust ejection model described below. The normalized production rate of 5 nm silica particles is shown in Extended Data Fig. 1c.

Dynamical evolution of charged nanoparticles. The predominant acceleration of charged nanoparticles in Saturn's magnetosphere stems from the outward-pointing co-rotation electric field[5,7,8,30]. In the first order, only positively charged dust particles gain energy and escape. Therefore, the fate of nanoparticles depends on the charging processes, that is, the plasma conditions at the location where they are released. Using the plasma model described previously, the ejection probability map of nanodust particles is simulated. See ref. 7 for the modelling details of the stochastic charging process and the equation of motion of nanoparticles.

Extended Data Fig. 2 shows the P_{eject} maps for 5 nm silica and water ice particles. A successful ejection event is defined as when the required ejection time of a test particle is less than half of its sputtering lifetime. The sputtering yield of water ice is about an order of magnitude larger than that of silicates (for example, $\Phi_{ice} \approx 1.5$ and $\Phi_{silicate} \approx 0.15$ for incident He ions at 500–1,000 eV energy range[26]). We assume that the sputtering lifetime for silica is ten times longer than that of water ice. The particle size decrease due to sputtering is not considered in the simulation[7].

The emission patterns. The dynamical properties of charged test nanoparticles released from the E ring simulated in the above step are converted to ER (equation (5) in ref. 7)) and the latitudinal emission pattern, weighted by the normalized production rate (equation (2)) according to their initial location, as shown in Extended Data Fig. 3a, b. We also modelled the emission patterns assuming that nanosilica particles are ejected directly from Enceladus, to examine our hypothesis (Extended Data Fig. 3c, d).

The nanosilica colloid concentration. f_{sp} in equation (1) can be determined by comparing the modelled stream particle production rate (w) with the CDA stream particle flux measurements, as shown in Fig. 4. The CDA observations are summarized in Extended Data Table 1. We assume that (1) f_{sp} and f_{eff} remain constant through the E-ring grains' lifetime, and (2) nanosilica particles are mixed homogenously in the ice matrix of E-ring grains (that is, $f_{eff} = 1$) so their release is directly proportional to the sputtering erosion rate. Figure 4 shows that the derived f_{sp} ranges from about 150 to 3,900 p.p.m. (parts per million), depending on the adopted E-ring size distribution slope. The conservative lower limit of the dissolved silica concentration at the reaction sites is about 210 p.p.m. (3.5 mM), including the silica solubility at 0 °C (~1 mM, or 60 p.p.m.). This corresponds to minimum reaction temperatures of 250 °C and 120 °C for solution pH values of 9 and 10, respectively (Fig. 2a).

Spectra analysis. *Data set.* The Cassini CDA measures the composition of individual dust grains by time of flight (TOF) mass spectroscopy[9]. Owing to the small mass of stream particles, their impact ionization spectra provide only weak particle mass lines at best[6,7]. In previous investigations[6,7] only Si^+ at 28u (u = unified atomic mass unit) could be identified as a definite particle constituent. Here we aim to go to the absolute detection limit possible with CDA. The goal is to quantify the most prominent elemental stream particle constituent, silicon[6,7], and to identify other elements that are typically abundant in silicate minerals (for example, magnesium or iron). Therefore only spectra with the best particle signals recorded between April 2004 and January 2008 were used for this analysis. The main reason to choose this period is that it provides the highest quality CDA spectra with the lowest possible contamination background. Starting in March 2008, CDA was frequently operating deep inside Enceladus' plume, during which time the refractory constituents of Enceladian ice grains, for example, sodium and potassium salts, might have accumulated and enhanced the CDA target contamination.

From the data set of over 2,000 stream particle spectra, 32 spectra with the highest signal-to-noise ratio of a 28u (±0.6u) signal were selected. A Si^+ signal amplitude of 0.7 μV was chosen as the selection threshold. This value provides clear Si^+ signals as well as a sufficiently large ensemble of spectra. These impact-ionization spectra also show relatively high total ion production (the sum of ions stemming from target material, target contamination and the particle itself). Thus, the selected spectra probably represent the largest detected stream particles at the highest encounter speeds during the observation time.

The selected spectra probably show the highest abundance of particle material (compared to target material and target contamination) and thus provide the highest probability of detecting further elemental particle constituents. Note that even in these spectra, ions from particle compounds only amount to about 1%. To further enhance the signal-to-noise ratio, the spectra were co-added and 'Lee' filtered (Fig. 1). Other exemplary spectra of stream particles can be found elsewhere[6,7].

Spectra interpretation. The selected impacts most probably occurred at speeds above 200 km s^{-1}. In this regime, the energy density is orders of magnitude higher than the molecular bond energies[35,36]. Therefore, similarly to the case of Jovian stream particles[37], only elemental ions are produced upon impact. However, subsequent clustering by collisions of neutral and ionized elements in the impact cloud (before the ions 'feel' the accelerating potential of the TOF spectrometer) can produce two-component ions[37]. In the case of the data set used for this work, this clustering

phenomenon is responsible for the formation of bi-elemental cations from the target material rhodium (Rh_2^+) (Fig. 1). The ratio of Rh^+/Rh_2^+ is about 100. Since rhodium is probably the most abundant constituent of the impact cloud, the intensity of this low-level signature marks the upper limit for the abundance of other non-elemental ions. This also helps to resolve the notorious ambiguity of the 28u signature in mass spectrometry that, besides silicon, can in principle be assigned to cations of N_2, CO, CNH_2 and C_2H_4. Carbon and hydrogen are highly abundant spectrum contaminants from the instrument target, these elements thus cannot be assessed with respect to the composition of stream particles[10]. Although all these components could potentially contribute to the 28u mass line, their abundance can be expected to be very low at most.

From integration of the spectral peaks, abundances and ratios of cationic species in the impact cloud can be directly derived. Ionization probabilities of the different species have to be considered to form conclusion regarding the composition of the particle. This is of particular relevance to reaching a conclusion about the metal to silicon ratio in stream particles, one of the main goals of the spectra analysis. All metals, especially Mg/Ca and Na/K, have a higher probability of forming cations than silicon[38]. The highest possible metal signal in the spectrum shown in Fig. 1 is a peak at an atomic mass of 23–24 u in agreement with sodium (Na^+) and/or magnesium (Mg^+; the adjacent mass lines can not be distinguished here), which is about 5 times less abundant than the Si^+ signature. Two regions with mass lines that can be attributed to K^+/Ca^+ at 39–40 u and unspecified species (at ~3.6 μs, or 56–60 u) are of weak significance, indicating even lower abundances if considered as particle constituents. In contrast to these metals, silicon is not completely converted from elements to cations. It has a higher ionization potential and higher electron affinity, which lead to simultaneous formation of anions, cations and neutrals in the impact cloud. Laboratory calibrations imply the cationization probability of Si to be about 3 times lower than that of Mg[39]. In total, Fig. 1 implies a metal to silicon ratio below 1/10. This ratio of the most metal-depleted silicates is 2/3 and ranges from 1 to 2 for most rock forming minerals. It is possible that traces of Na and K have been transferred to the surface of nanosilica particles from remains of salt-rich carrier ice grains causing the weak signatures at mass 23u and 39u. We note that the observed possible metal signatures are upper limits for the particle constituents, as the CDA target is known to have a low-level contamination of Na and K (ref. 10). A bi-elemental cluster (C_2^+, 24u), formed from the highly abundant carbon contamination, might also significantly contribute to the signal at mass 23–24. Consequently it is possible that the potential weak metal mass lines stem entirely from contamination, and that stream particles are entirely metal-free. To summarize, while we cannot completely rule out that some of the weak signatures have contributions from metal ions stemming from the particle, their abundance is far too low to be in agreement with a rock-forming silicate.

In Fig. 1 the O^+/Si^+ ratio is about 2. However, in contrast to metals, oxygen has a lower probability of forming cations than does silicon. Therefore, the O^+/Si^+ ratio should be clearly below 2 for a pure silica (SiO_2) particle. From laboratory calibration we expect it to be around 1. But as oxygen is known to be a target contaminant that contributes to the O^+ mass line to an unknown extent[10], the observed ratio is consistent with SiO_2.

Stream particle size estimate by integration of the Si^+ signal. By integrating the strongest Si^+ signals, the number of Si^+ ions created by the impinging particle can be calculated. The idea that the impact ionizes all Si atoms is a simplification, but in the case of ultra-fast stream particles it is probably sufficiently accurate to infer a meaningful lower limit for the number of Si atoms in the particle. This in turn allows for mass and size calculation, again a lower limit, if stream particles are assumed to consist solely of SiO_2.

The integrated signal of the Si^+ peak in Fig. 1 is equivalent to about 1,500 ions. As explained above, this signal probably stems from the largest measured stream particles at the highest encounter speed (>200 km s^{-1})[40]. The ions recorded in CDA mass spectra represent about 1/6.5 of the ions that were initially formed[9]. We conclude that the largest stream particles created about 10,000 Si cations upon impact.

Under the assumption of a pure spherical SiO_2 particle, we can now calculate a size from this number. If we want to derive a strict lower limit on the largest particle size, we have to assume a grain built of about 10,000 SiO_2 molecules, which leads to a particle radius of about 6 nm, if we assume a density of 2,200 kg m^{-3} for amorphous silica. As mentioned above, it is highly probable that only a fraction of silicon is converted into cations even at the extreme impact speed of stream particles. A more realistic assumption is that only a third of Si atoms form cations, which gives a maximum particle radius of about 8.5 nm (for comparison, the largest Jovian stream particles reach radii of over 20 nm; refs 8, 37).

Hydrothermal experiments and calculations. We performed hydrothermal experiments based on the methodology and apparatus employed in previous studies[41–43]. The starting mineral powder and solution were introduced into a flexible gold reaction cell, pressurized to 400 bar with a steel alloy autoclave[41]. The pressure condition corresponds to that of Enceladus' rocky core (~150 km below the water–rock interface). The effect of pressure is not critical for estimating the temperature required for nanosilica formation. This is because the silica concentration equilibrated by the serpentine-talc/saponite buffer is not sensitive to pressure range within the core (~100–500 bar)[44]. The flexible gold reaction cell consists of a gold reaction bag and a titanium head[41], which was oxidized before use. The flexible reaction cell allows us to perform an on-line collection of fluid samples during the experiments[41–43]. See ref. 41 for more details.

As starting minerals, we used a mixture of powdered olivine (San Carlos Olivine: $Mg_{1.8}Fe_{0.2}SiO_4$) and orthopyroxene ($MgSiO_3$) (orthopyroxene: olivine = 7: 3 by weight; 15 g in total). These are major minerals known to be abundant in asteroids and comets[45,46]. San Carlos olivine contains trace amounts of spinel and pyroxene, which were the source of Al, Ca and other elements. We synthesized orthopyroxene crystals using the flux method[47,48]. The starting solution (~ 60 g) was an aqueous solution of NH_3 (1.1 mol per kg H_2O) and $NaHCO_3$ (360 mmol per kg H_2O).

We conducted two experiments at different temperatures. One was performed at a constant temperature of 300 °C for ~2,700 h of reaction time. In the other experiment, the temperature was set to 120 °C for an initial ~1,700 h of reaction time, and then increased to 200 °C (~2,300 h of reaction time in total). We measured the concentrations of dissolved silica and other major elements (for example, Na, Mg, Fe, Ca, Al and K) dissolved in the fluid samples during the reaction time with inductively coupled plasma atomic emission spectroscopy (Perkin Elmer). Mineralogical analyses for the solids collected after the experiments were performed with an X-ray diffraction spectrometer (X'PERT-PRO PANalytical). The *in situ* pH of the solution in the experiments was calculated using the measured pH of the fluid samples at room temperature and concentrations of dissolved gas and elements. The *in situ* pH values are calculated as 8.4–8.8, whereas measured pH values at room temperature were 10.1–10.2 at the end of the experiments.

The ΣSiO_2 concentration determined by chemical equilibrium between serpentine and talc/saponite was calculated with equilibrium constants computed with the SUPCRT92 program[49]. Given the similarity in the chemical compositions between talc and saponite, we used the thermodynamic data of talc in the calculations. The solubility of silica at 0 °C was calculated from thermodynamic data of amorphous silica. The concentrations of $HSiO_3^-$ and $NaHSiO_3$(aq.) were calculated for different pH values and at 0.1 mol per kg Na^+ concentration using the equilibrium constants of the following reactions: $SiO_2(aq.) + H_2O \leftrightarrow HSiO_3^- + H^+$ and $HSiO_3^- + Na^+ \leftrightarrow NaHSiO_3(aq.)$.

We observed silica nanoparticle formation by cooling the fluid samples collected in the experiments at 300 °C. A part of the sample was cooled at ~0 °C in an ice bath, and then dialysis treatment (that is, fluid removal) was performed for several minutes. After the dialysis, a drop of the sample was mounted on a slide, and the excess solution was wicked away with tissue paper. Microscopic observations of the slide were performed with a field emission scanning electron microprobe (FE-SEM). Individual and clustered silica nanoparticles were observed (Fig. 2). The typical size of individual particles was ~5–20 nm in diameter. The energy dispersive spectrum indicates that they are composed mainly of Si and O with trace amounts of Na and Ca (Extended Data Fig. 4), which may be adsorbed on the surface of particles.

Timescale of growth of nanosilica in Enceladus' ocean. We estimated this on the basis of the equation shown in the previous study[21]. The primary size of nanosilica formed from alkaline aqueous solution is a few nanometres in radius[12,14–17]. After the formation of these nanosilica particles, the size would increase slowly by precipitation of dissolved silica onto the surface (Ostwald ripening)[12]. The timescale of growth, t_g, of radius from r_s to r by Ostwald ripening in pure water can be described as follows (equation (14) in ref. 21);

$$t_g = r^2 S_0(T_0) / R_0 r_s S_0(T)$$

where R_0 is the dissolution rate of silica, and $S_0(T)$ and $S_0(T_0)$ are the solubility of silica at a given temperature, T, and that at the temperature, T_0, where the experimental data were obtained (25 °C), respectively. According to the previous study[50], R_0 for amorphous silica is 8.8×10^{-15} cm s^{-1} at 0 °C. The ratio of $S_0(T_0)/S_0(T)$ is calculated as 1.67 for $T = 0$°C (ref. 21). Thus, the timescale for a 2-nm-sized nanosilica particle to grow to an 8-nm-sized particle at 0 °C in pure water is estimated as ~20 years. If NaCl is included in the solution, the Ostwald ripening proceeds more rapidly, about 10–100 times faster than in pure water[50]. Thus, the nanosilica particles with radius of ≤8 nm, observed by Cassini CDA, should have been formed within months to years, suggesting continuing hydrothermal activity in Enceladus.

Enceladus' silicon footprint in Saturn's magnetosphere. After being transported to the near-surface plume sources, nanosilica particles eventually become grain inclusions in frozen water droplets[1,2,22] from spray above Enceladus' subsurface liquid plume sources—or they may entrain in the gas flow and serve as condensation seeds in the vent. After entering the E ring they are exposed to Saturn's magnetosphere, separated from ice grains by differential plasma sputtering erosion and eventually ejected into interplanetary space as stream particles.

About 1 mM (60 p.p.m.) of silica might in fact still be dissolved in liquid Enceladus plume sources at 0 °C and become an additional ice grain constituent upon freezing. After sputtering erosion and ionization, this component, as well as erosion of nanosilica particles, contributes to the mass 28 ions observed by the Cassini plasma instruments CAPS (Cassini Plasma Spectrometer)[51] and MIMI (Magnetospheric Imaging Instrument)[52] at different energies.

Analysis of CAPS ion measurements[51] shows that the density ratio between the mass 28 and water group ions is about 6×10^{-5}, which corresponds to a mass fraction of ~90 p.p.m. and interestingly is comparable to silica solubility at 0 °C (50 and 120 p.p.m. for pH = 9 and 10, respectively). The mass resolution of Cassini instruments cannot distinguish between $HCNH^+$, CO^+, N_2^+ or Si^+, and therefore no solid conclusion can be drawn for the origin of the mass 28 ions at the current stage[52]. The sputtering yield of Si-water ice mixture is unknown. Nonetheless, the presence of nanosilica particles and ice grains forming from hydrothermal fluids surely will supply the magnetosphere with silicon ions. Future modelling efforts should focus on the ionization, ion lifetime and acceleration processes that may be responsible for the enhanced ratio of $^{28}M^+$ to water-group ions, $(3–7) \times 10^{-3}$, at the 100 keV energy level[52].

Sample size. In data analyses above, no statistical methods were used to predetermine sample size.

26. Tielens, A. G. G. M. *et al.* The physics of grain-grain collisions and gas-grain sputtering in interstellar shocks. *Astrophys. J.* **431,** 321–340 (1994).
27. Spahn, F. *et al.* Cassini dust measurements at Enceladus and implications for the origin of the E ring. *Science* **311,** 1416–1418 (2006).
28. Horányi, M., Burns, J. & Hamilton, D. G. Dynamics of Saturn's E ring particles. *Icarus* **97,** 248–259 (1992).
29. Horányi, M., Juhász, A. & Morfill, G. E. Large-scale structure of Saturn's E-ring. *Geophys. Res. Lett.* **35,** L04203 (2008).
30. Horányi, M. Dust streams from Jupiter and Saturn. *Phys. Plasmas* **7,** 3847–3850 (2000).
31. Burton, M. E., Dougherty, M. K. & Russell, C. T. Saturn's internal planetary magnetic field. *Geophys. Res. Lett.* **37,** L24105 (2010).
32. Jurac, S., Johnson, R. E. & Richardson, J. D. Saturn's E ring and production of neutral torus. *Icarus* **149,** 384–396 (2001).
33. Johnson, R. E. *et al.* Sputtering of ice grains and icy satellites in Saturn's inner magnetosphere. *Planet. Space Sci.* **56,** 1238–1243 (2008).
34. Shi, M. *et al.* Sputtering of water ice surfaces and the production of extended neutral atmospheres. *J. Geophys. Res.* **100,** 26387–26395 (1995).
35. Hornung, K. & Kissel, J. On shock wave impact ionization of dust particles. *Astron. Astrophys.* **291,** 324–336 (1994).
36. Hornung, K., Malama, Y. & Kestenboim, K. Impact vaporization and ionization of cosmic dust particles. *Astrophys. Space Sci.* **274,** 355–363 (2000).
37. Postberg, F. *et al.* Composition of Jovian dust stream particles. *Icarus* **183,** 122–134 (2006).
38. Stephan, T. TOF-SIMS in cosmochemistry. *Planet. Space Sci.* **49,** 859–906 (2001).
39. Fiege, K. *et al.* Compositional analysis of interstellar dust as seen by the Cassini Cosmic Dust Analyser. In *76th Annual Meteoritical Society Meeting,* http://www.hou.usra.edu/meetings/metsoc2013/pdf/5087.pdf (2013).
40. Hsu, H.-W. *et al.* Probing IMF using nanodust measurements from inside Saturn's magnetosphere. *Geophys. Res. Lett.* **40,** 2902–2906 (2013).
41. Shibuya, T. *et al.* Reactions between basalt and CO_2-rich seawater at 250 and 350°C, 500 bars: implications for the CO_2 sequestration into the modern oceanic crust and composition of hydrothermal vent fluid in the CO_2-rich early ocean. *Chem. Geol.* **359,** 1–9 (2013).
42. Seyfried, W. E. Jr, Foustoukos, D. I. & Fu, Q. Redox evolution and mass transfer during serpentinization: an experimental and theoretical study at 200°C, 500 bar with implications for ultramafic-hosted hydrothermal systems at mid-ocean ridges. *Geochim. Cosmochim. Acta* **71,** 3872–3886 (2007).
43. McCollom, T. M. & Seewald, J. S. Experimental constraints on the hydrothermal reactivity of organic acids and acid anions: I. Formic acid and formate. *Geochim. Cosmochim. Acta* **67,** 3625–3644 (2003).
44. Vance, S. *et al.* Hydrothermal systems in small ocean planets. *Astrobiology* **7,** 987–1005 (2007).
45. Nakamura, T. *et al.* Chondrulelike objects in short-period comet 81P/Wild 2. *Science* **321,** 1664–1667 (2008).
46. Brearley, A. J. in *Meteorites and the Early Solar System II* (eds Lauretta, D. S. & McSween, H. Y.) 587–624 (Univ. Arizona Press, 2006).
47. Ozima, M. Growth of orthoenstatite crystals by the flux method. *J. Jpn Assoc. Mineral. Petrol. Econ. Geol.* **3** (suppl), 97–103 (1982); in Japanese with English abstract.
48. Tachibana, S., Tsuchiyama, A. & Nagahara, H. Experimental study of incongruent evaporation kinetics of enstatite in vacuum and in hydrogen gas. *Geochim. Cosmochim. Acta* **66,** 713–728 (2002).
49. Johnson, J. W., Oelkers, E. H. & Helgeson, H. C. SUPCRT92: a software package for calculating the standard molal thermodynamic properties of minerals, gases, aqueous species, and reactions from 1 to 5000 bar and 0 to 1000°C. *Comput. Geosci.* **18,** 899–947 (1992).
50. Icenhower, J. P. & Dove, P. M. The dissolution kinetics of amorphous silica into sodium chloride solution: effects of temperature and ionic strength. *Geochim. Cosmochim. Acta* **64,** 4193–4203 (2000).
51. Martens, H. R. *et al.* Observations of molecular oxygen ions in Saturn's magnetosphere. *Geophys. Res. Lett.* **35,** L20103 (2008).
52. Christon, S. P. *et al.* Saturn suprathermal O_2^+ and mass-28^+ molecular ions: long-term seasonal and solar variation. *J. Geophys. Res.* **118,** 3446–3463 (2013).
53. Kempf, S. *et al.* The electrostatic potential of E ring particles. *Planet. Space Sci.* **54,** 999–1006 (2006).

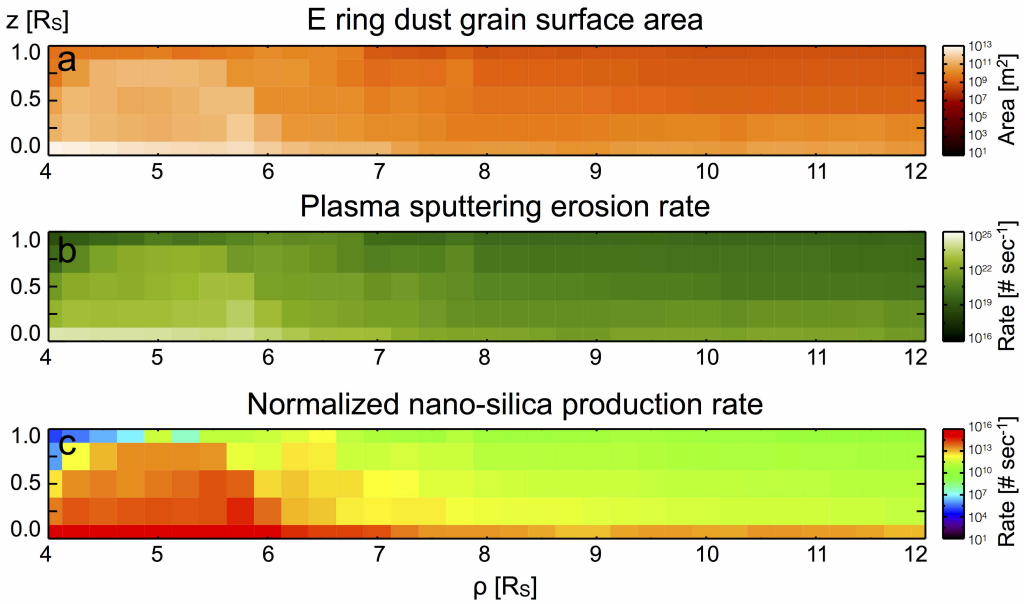

Extended Data Figure 1 | Maps of grain density, sputtering erosion rate, and stream particle production rate in the E-ring region. **a**, The total E-ring ice grain surface area map in the ρ–z frame, where ρ and z are distance to Saturn's rotation axis and to the ring plane, respectively. Note that each bin integrates azimuthally over the entire torus, meaning that the outer bins contain a much larger volume than do the inner ones. **b**, Plasma sputtering erosion rate of E-ring ice grains in torus segments. The total sputtering rate is 8.6×10^{24} H_2O molecules per second, lower but still comparable to the 4.5×10^{25} H_2O molecules per second derived in ref. 32. **c**, Normalized nanoparticle production rate in particles per second. R_S, Saturn radius.

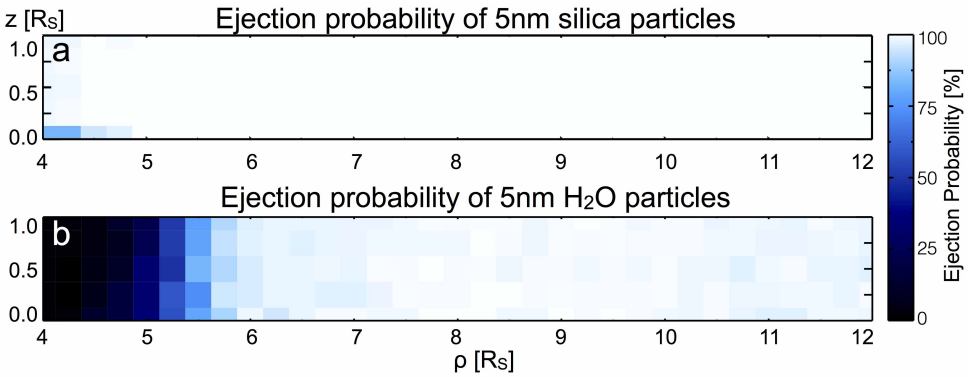

Extended Data Figure 2 | Ejection probability of 5-nm particles from the E ring. **a**, For silica nanoparticles, the ejection probability is mostly close to unity (except within $4.5R_S$). The higher local plasma density there leads to negative dust potential and thus reduces the ejection probability[7]. The typical timescale for silica nanoparticles to acquire sufficient kinetic energy to escape is of the order of a day[7]. **b**, Water ice nanoparticles have lower secondary emission and are charged less positively and thus are less likely to be ejected. This 'forbidden region' (the black region) extends further outward to $\sim 5.5\,R_S$, consistent with the CDA measurements[53].

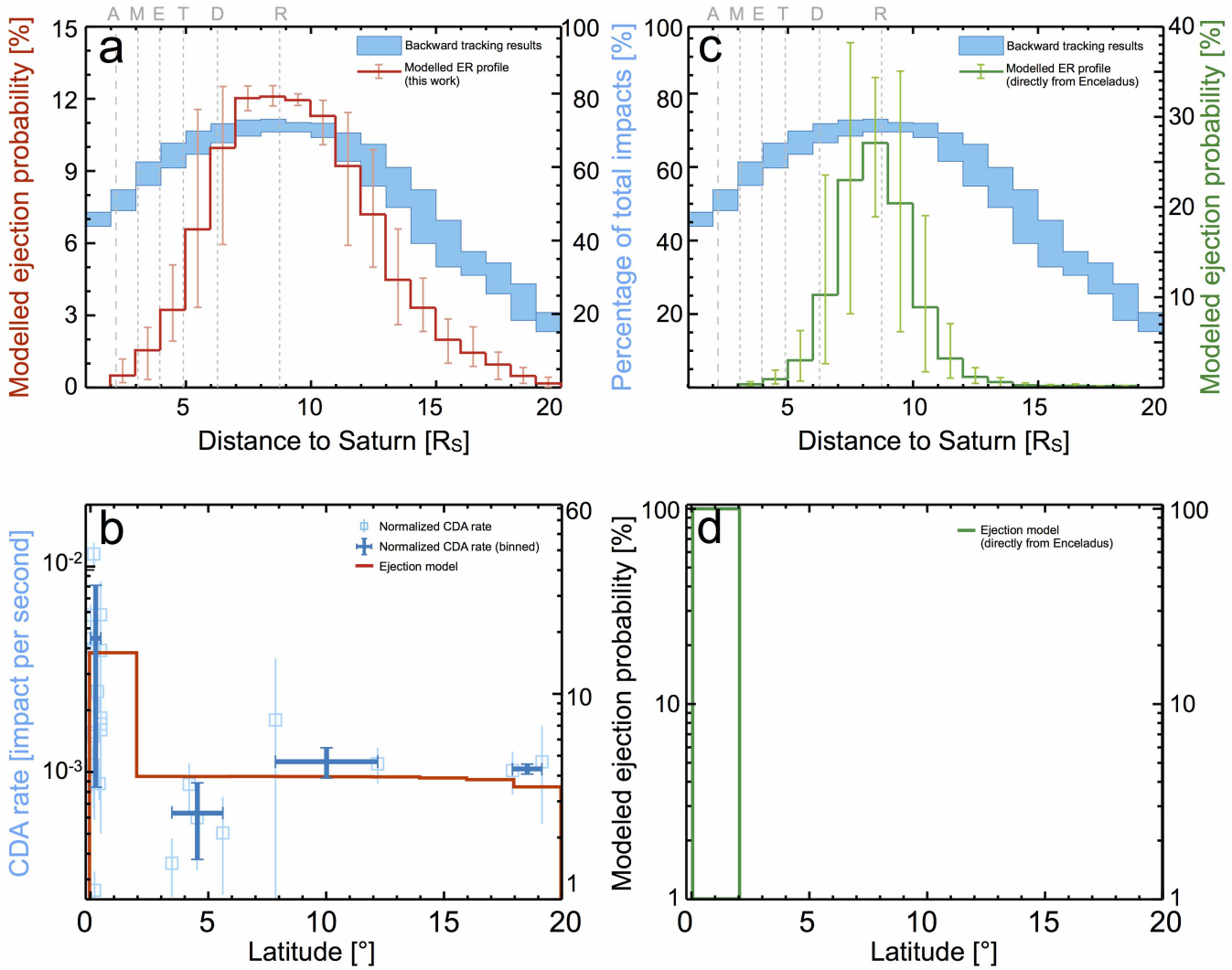

Extended Data Figure 3 | Stream particle emission patterns. **a**, Ejection region (ER) profiles, derived from the nanodust and solar wind measurements (blue)[7] and the ejection model (red), both peak at 7–9R_S. The uncertainty of both profiles stems from the adopted co-rotation fraction of Saturn's magnetosphere (80–100%), which determines the electromagnetic acceleration amplitude. The location of the outer rim of Saturn's A ring and the orbits of icy satellites are marked by grey dashed lines. **b**, Latitudinal-dependent ejection pattern. Scatter and binned stream particle rates (normalized to 25R_S distance) are shown in blue squares and crosses, respectively. The vertical length of the crosses represents the standard deviation of the stream particle rate in the corresponding bin. Our model (red) reproduces the measured trend. **c**, **d**, Modelled patterns assuming direct ejection from Enceladus. While the ER profile is similar, these particles are only ejected along the ring plane.

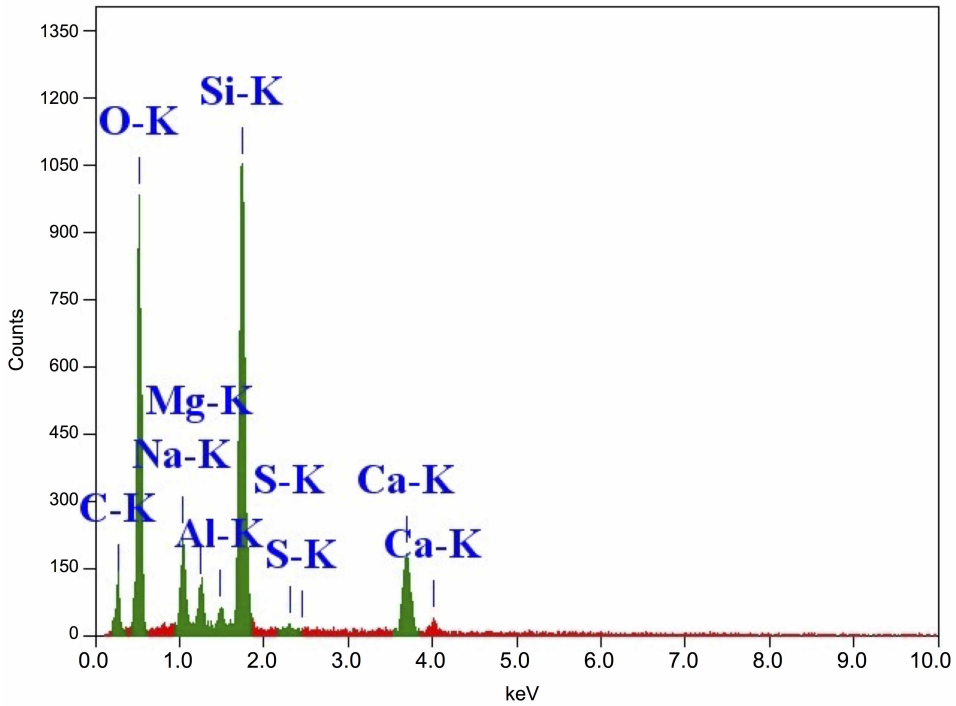

Extended Data Figure 4 | Energy dispersive spectrum of clustered silica nanoparticles formed from the fluid sample. See Methods for details.

Extended Data Table 1 | Stream particle flux measurements

UTC (medium)	Dur. (minute)	Dist. (R_S)	Lat. (°)	Impacts	Impact rate (# second^{-1})	Production rate (# second^{-1})
2004-346T01:05	280	36.4	-5.62	4	2.4×10^{-4}	8.6×10^{17}
2004-347T13:40	579	28.0	-3.45	10	2.9×10^{-4}	1.2×10^{17}
2004-348T22:25	585	18.0	0.17	18	5.1×10^{-4}	9.1×10^{16}
2005-063T00:07	541	38.2	-0.10	15	4.6×10^{-4}	3.7×10^{17}
2005-084T18:55	135	33.5	-0.14	18	2.2×10^{-3}	1.4×10^{18}
2005-084T23:25	204	32.8	-0.14	15	1.2×10^{-3}	7.2×10^{17}
2005-085T23:25	187	28.1	-0.17	8	7.1×10^{-4}	3.1×10^{17}
2005-099T05:15	564	36.3	-4.19	14	4.1×10^{-4}	3.0×10^{17}
2005-100T00:00	264	34.5	-4.52	5	3.1×10^{-4}	2.1×10^{17}
2005-228T16:05	464	31.4	-17.9	18	6.5×10^{-4}	1.9×10^{18}
2005-282T10:50	114	25.8	-0.30	16	2.3×10^{-3}	8.4×10^{17}
2005-330T11:50	204	13.9	-0.37	35	2.8×10^{-3}	3.0×10^{17}
2005-336T21:45	319	39.0	-0.02	35	1.8×10^{-3}	1.5×10^{18}
2006-116T17:18	187	24.2	-0.14	18	1.6×10^{-3}	5.1×10^{17}
2006-136T05:23	86	40.9	0.14	3	5.8×10^{-4}	5.3×10^{17}
2006-146T17:20	150	35.9	0.44	7	7.8×10^{-4}	5.5×10^{17}
2006-147T12:50	50	40.1	0.43	2	6.7×10^{-4}	5.9×10^{17}
2006-147T16:55	191	40.6	0.43	8	6.9×10^{-4}	6.3×10^{17}
2006-261T04:35	858	37.6	12.2	25	4.9×10^{-4}	2.0×10^{18}
2006-308T04:35	75	28.1	19.2	4	8.9×10^{-4}	2.1×10^{18}

Twenty observations obtained when Saturn was within 28° of the CDA bore-sight were selected. 278 impacts were registered during the total 100.8 h observation time. Data showing the flux enhancement caused by solar wind–nanodust interactions[8,40] were excluded. The impact rate is normalized to a Saturn distance of 25 R_S (inverse-square law) and is converted to production rate by the modelled flux–latitude relation (Extended Data Fig. 3b). The weighted production rate is $(8.3 \pm 6.3) \times 10^{17}$ particles per second, corresponding to 1.0 ± 0.7 g per second (assuming a mean particle radius of 5 nm). UTC (medium), medium time of observation in Coordinated Universal Time; Dur., duration; Dist., distance; Lat, latitude.